JGR Space Physics

RESEARCH ARTICLE
10.1029/2020JA027880

Special Section:
Early results from the Global-scale Observations of the Limb and Disk (GOLD) mission

New Observations of Large-Scale Waves Coupling With the Ionosphere Made by the GOLD Mission: Quasi-16-Day Wave Signatures in the F-Region OI 135.6-nm Nightglow During Sudden Stratospheric Warmings

Quan Gan[1], Richard W. Eastes[1], Alan G. Burns[2], Wenbin Wang[2], Liying Qian[2], Stanley C. Solomon[2], Mihail V. Codrescu[3], and William E. McClintock[1]

[1]Laboratory of Atmospheric and Space Physics, University of Colorado Boulder, Boulder, CO, USA, [2]High Altitude Observatory, National Center for Atmospheric Research, Boulder, CO, USA, [3]Space Weather Prediction Center, National Oceanic and Atmospheric Administration, Boulder, CO, USA

Key Points:
- Significant quasi-16-day oscillations (Q16DOs) were observed in the OI 135.6-nm nightglow by GOLD
- The Q16DOs in nightglow are closely correlated with quasi-16-day wave (Q16DW) activities in the middle atmosphere
- The EIA crests showed antisymmetric Q16DOs between the two hemispheres likely driven by Q16DW-modulated tides

Correspondence to:
Q. Gan,
blondganquan@gmail.com

Citation:
Gan, Q., Eastes, R. W., Burns, A. G., Wang, W., Qian, L., Solomon, S. C., et al. (2020). New observations of large-scale waves coupling with the ionosphere made by the GOLD Mission: Quasi-16-day wave signatures in the F-region OI 135.6-nm nightglow during sudden stratospheric warmings. *Journal of Geophysical Research: Space Physics*, *125*, e2020JA027880. https://doi.org/10.1029/2020JA027880

Received 4 FEB 2020
Accepted 17 MAR 2020
Accepted article online 4 APR 2020

©2020. The Authors.
This is an open access article under the terms of the Creative Commons Attribution License, which permits use, distribution and reproduction in any medium, provided the original work is properly cited.

Abstract The recently launched Global-scale Observations of the Limb and Disk (GOLD) Mission observed prominent quasi-16-day oscillations (Q16DOs) in the OI 135.6-nm nightglow from the equatorial ionization anomaly (EIA) region during 26 November 2018 to 25 January 2019. Meanwhile, the enhanced and concurrent quasi-16-day wave (Q16DW) activity was observed in the middle atmosphere by the Sounding of the Atmosphere using Broadband Emission Radiometry (SABER) instrument. This implies that the F-region ionosphere couples with the lower atmosphere through large-scale waves. A noteworthy phenomenon was that the Q16DOs displayed an asymmetric behavior between the northern and southern EIA crests. This asymmetry indicates that the ionospheric Q16DOs might be driven by the Q16DW-modulated tides, which not only modulated the E-region dynamo winds but also modulated the F-region field-aligned neutral winds via vertical penetration, producing the oscillations in plasmas densities.

Plain Language Summary Driving of the short-term variability in the ionosphere is a crucial scientific question of space physics, which connects the thermosphere and ionosphere to the solar and magnetospheric forcing, as well as terrestrial atmosphere weather. It is also the most challenge part of space weather forecast. Traveling planetary waves (PWs), including the eastward propagating Kelvin waves and westward propagating Rossby waves, are responsible for a large amount of day-to-day variability in ionospheric parameters. Our study showed an evidence of the Rossby waves coupling with the nighttime F-region ionosphere observed by GOLD. More importantly, the observations suggested a physical pathway accounting for the PW coupling in the atmosphere-ionosphere system; that is, PW-modulated tides penetrate into the F-region ionosphere and produce the field-aligned motion of the plasmas, leading to the oscillations in electron density at the PW periods.

1. Introduction

It is understood that F-region ionosphere is regulated by the forcing from the Sun, the magnetosphere (e.g., Forbes et al., 2000; Lei et al., 2008; Rishbeth & Mendillo, 2001), and the lower atmosphere (e.g., Akmaev, 2011; Liu, 2016; Oberheide et al., 2015; Sassi et al., 2019; Vincent, 2015). During solar and geomagnetically quiet times, a considerable amount of day-to-day ionospheric variability is due to traveling planetary waves (PWs) in the lower atmosphere, including eastward-propagating equatorial Kelvin waves and westward-propagating Rossby waves (Altadill, 2000; Borries & Hoffmann, 2010; Forbes et al., 2018; Lastovicka, 2006; Yi & Chen, 1993; and references therein). The latter are also called "normal modes (NM)", typically having periods of 2–20 days and zonal wavenumbers of 1–4, which are the global solutions of the Laplace's tidal equation (Salby, 1981, 1984). In the recent literature, several well-known PWs were widely referred to as "Q2DW," "Q6DW," "Q10DW," and "Q16DW" (the numbers stand for the wave periods; Q, D, and W are the acronym of "quasi-," "day," and "wave," respectively). Over the past decade,

considerable advances have been made in delineating the global morphology of PW-induced signatures in the ionosphere and the understanding of physical mechanisms by which the PW signatures are transmitted into the F-region heights (Chang et al., 2010, 2014; Gan et al., 2015, 2016, 2017, 2018; Pedatella & Forbes, 2012; Yamazaki et al., 2018; Yue et al., 2013, 2016; Yue & Wang, 2014; and references therein). However, those studies are primarily focused on the wave components with relatively shorter wave periods (i.e., 2, 3–4, and 6 days) but larger phase speeds and vertical wavelengths.

The quasi-16-day wave (Q16DW) is recognized as the second symmetric mode (1, −4) of zonal wavenumber 1 Rossby waves. It is usually enhanced at midlatitude and high latitude in the winter hemisphere (Day et al., 2011). The observed 16-day wave can, to some extent, depart from the theoretical prediction because the latter assumes the ideal atmosphere, that is, isothermal, windless, and dissipationless. Other than the significant role in the middle atmosphere dynamics, the Q16DW also induces periodic variations in the ionosphere. Early studies have used ionosonde measurements, establishing a connection between the quasi-16-day oscillations (Q16DOs) in the F_2-region ionosphere and the Q16DWs in the mesospheric winds (Forbes, 1996; Forbes et al., 1995; Forbes & Leveroni, 1992; Mendillo et al., 2002; Rishbeth & Mendillo, 2001; Yi & Chen, 1993). From a satellite observation perspective, Pedatella and Forbes (2009) showed a global picture of the Q16DW-induced oscillations in electron densities using CHAMP (Challenging Minisatellite Payload) data. Based on a linear spectral model, Forbes et al. (1995) suggested that the Q16DW is not able to penetrate to altitudes above 100 km, and the coupling is more than likely indirect. The probable candidates include the upward propagating tides and dissipated gravity waves (Meyer, 1999) that are modulated by the Q16DWs. The recently launched Global-scale Observations of the Limb and Disk (GOLD) mission provides an excellent opportunity to revisit this significant and recurrent but not fully understood phenomenon from a new perspective.

This study aimed at looking for the periodicity in the F-region equatorial ionization anomaly (EIA) during boreal winter in 2018/2019, when a sudden stratospheric warming (SSW) event occurred in the Northern Hemisphere and PWs were rather active. This thus provided an excellent opportunity to explore the wave coupling in the atmosphere-ionosphere system. Section 2 overviews the data used in this study. Section 3 presents the major findings. Section 4 is the conclusions.

2. Data Sets

The NASA (National Aeronautics and Space Administration) GOLD mission flies a far ultraviolet imager onboard the SES-14 satellite in the geostationary orbit. It has two identical channels, and each one scans one third of the Earth (roughly 120°W–20°E and 60°S–60°N) every 30 min. The imager is a spectrometer which monitors the OI 135.6 nm and the molecular nitrogen LBH bands emissions. These are used to retrieve the thermospheric daytime O/N_2 ratio, temperature, and nighttime peak electron density (Nmax) on the disk. In this study, we used the nighttime OI 135.6-nm emission data from GOLD disk scans measured by two channels simultaneously. The nighttime 135.6-nm emission produced by the ionosphere recombination peaks in the F_2-region where the electron density maximizes. The L1C data (version 3) and documentation guide are available at http://gold.cs.ucf.edu. We refer readers to Eastes et al. (2017, 2019) for a detailed description of GOLD instruments and the nighttime data product. Employing the daytime disk scans, Gan et al. (2020) showed a remarkable thermospheric response to a moderate geomagnetic storm.

Sounding of the Atmosphere using Broadband Emission Radiometry (SABER) onboard the Thermosphere Ionosphere Mesosphere Energetics and Dynamics (TIMED) satellite is a 10-channel broadband radiometer covering the spectral range from 1.27 to 17 μm. It provides temperature profiles retrieved from two 15-μm and one 4.3-μm CO_2 radiometer channels in a tangent height range spanning approximately 20–110 km. Remsberg et al. (2008) assessed the quality of version 1.07 temperature data and suggested that the systematic error is no more than 2 K below 70 km, while in the upper mesosphere and lower thermosphere region, the error increases with altitude from 1.8 K at 80 km to 6.7 K at 100 km. The effective vertical resolution of SABER temperature is approximately 2 km. SABER is in a slowly precessing polar orbit. The sampled local time shifts ~12 min on a daily basis, allowing approximately 24-hr local time coverage every 60 days at low to middle latitudes when both ascending and descending samples are combined. Due to the line of sight of SABER and the yaw maneuver of the TIMED satellite, the latitude coverage of SABER data is from 53°

latitude in one hemisphere to 83° in the other. In the current work, the latest version 2.0 temperature data were utilized to trace PW activity in the stratosphere and mesosphere.

3. Results and Discussion

Figure 1a displays the time series of the Kp (blue) and F10.7 (red) indices between 26 November 2018 and 24 February 2019. The time span covers the boreal winter, during which wave activity was significantly enhanced, to facilitate an investigation of wave impacts from the lower atmosphere on the thermosphere-ionosphere system. Wavelet analyses were performed on Kp and F10.7 indices to examine the periodic forcing by geomagnetic field and solar extreme ultraviolet band radiation, which may also induce ionospheric oscillations at the PW periods (Lei et al., 2008; Pedatella et al., 2010). It turns out that Kp (Figure 1b) was dominated by the 24-day and 8–9-day oscillations, whereas a ~24-day oscillation was evident in F10.7 (Figure 1c). This means that ionospheric oscillations associated with PWs, particularly those having a period of 10–20 days, are distinguishable during the given period. Figure 1d displays the zonally averaged zonal winds (red curve) and temperature (blue curve) at 30 hPa and 60°N. Note that the westerly jet of ~30 m/s decreased rapidly after day 25 (21 December) and the zonal winds reversed to weak easterlies (wind velocities <10 m/s) between day 35 and day 52 (31 December to 16 January 2019). Then, the zonal winds tended to return to their normal state. Such a disturbance in zonal winds is consistent with the well-defined SSW phenomenon, which is characterized by the polar vortex weakening due to enhanced PW activity. Moreover, the zonally averaged temperature increased by ~10–15 K during days 22–40. SSW events provide a suitable condition for the vertical propagation and amplification of PWs. As such, potential impacts of PWs on the ionosphere are achievable, for example, through the nonlinear interaction with tides or altering the tidal vertical wavelength (Chang et al., 2011; Gan et al., 2017; Liu et al., 2010).

Figure 2a displays a GOLD image of the OI nighttime 135.6-nm emission at 23:50 UT on 2 December 2018. The spatial coverage was roughly over the eastern America and western Atlantic Ocean. The EIA bands stood out with increased brightness toward the terminator. The peak brightness was of ~40 Rayleigh (R) over the South American sector, consistent with that reported by Eastes et al. (2019). The same GOLD image is illustrated in Figure 2b but smoothed to 3° (longitude) × 3° (latitude) in the quasi-dipole magnetic coordinate system (Richmond, 1995). The two crests of the EIA were located at around 10° and −15° magnetic latitudes, indicating a hemispheric asymmetry about the dip equator. In order to determine the periodicities in the OI 135.6-nm emission, the time series of brightness at 20°1 magnetic longitude (averaged over the longitudinal bin centered at 20° with 5° offset) is shown in Figure 2c. The brightness in the northern crest region demonstrated an oscillating pattern; that is, the higher brightness occurred on ~day 7, 22, and 39, while the brightness was relatively lower between those days in the same region.

Next, an empirical orthogonal function (EOF) analysis was performed on the time series to identify the predominant oscillations and their latitudinal dependence. The first 10 EOF modes were derived simultaneously, but only the EOF1 and EOF2 are illustrated here since they account for 56.6% and 21.0% of the total variability. The rest of the EOFs had an individual contribution to the total variability of less than 10% and did not show any periodicities connected to the PWs of interest. Figure 2d displays the latitudinal structure of the EOF1, describing the symmetric brightness changes about the dip equator between the two crests. The amplitude in the crest regions is of 0.2–0.25, greater than that over the magnetic equator by a factor of ~4. The temporal behavior of the EOF1 is described in Figure 2e, which showed an oscillation of ~60 days during the given period. Specifically, the brightness was enhanced (weakened) before (after) day 25. Several reasons are likely responsible for this tendency in brightness. First, the F_2-layer peak electron density has a strong seasonal dependence in the EIA region, maximizing at around December solstice and decreasing afterward (Qian et al., 2013). Since the nighttime OI 135.6-nm brightness is produced by recombination, the brightness change is intimately related to the change of electron densities. Second, we note that the moment when the brightness change in Figure 2e turned over from positive to negative was aligned with the onset of the weakened polar vortex (day 25). This implies that the brightness depletion after day 25 (21 December 2018) may also be associated with the SSW. Pedatella et al. (2016) suggested that an enhanced migrating semidiurnal tide (SW2) during SSW events is able to induce a global-scale upward circulation and thereby a reduction of zonal mean O/N_2 ratio and electron densities (Liu & Roble, 2002; Oberheide et al., 2020; Shepherd et al., 1999). In addition, the intraseasonal variability (e.g., Sassi et al., 2019;

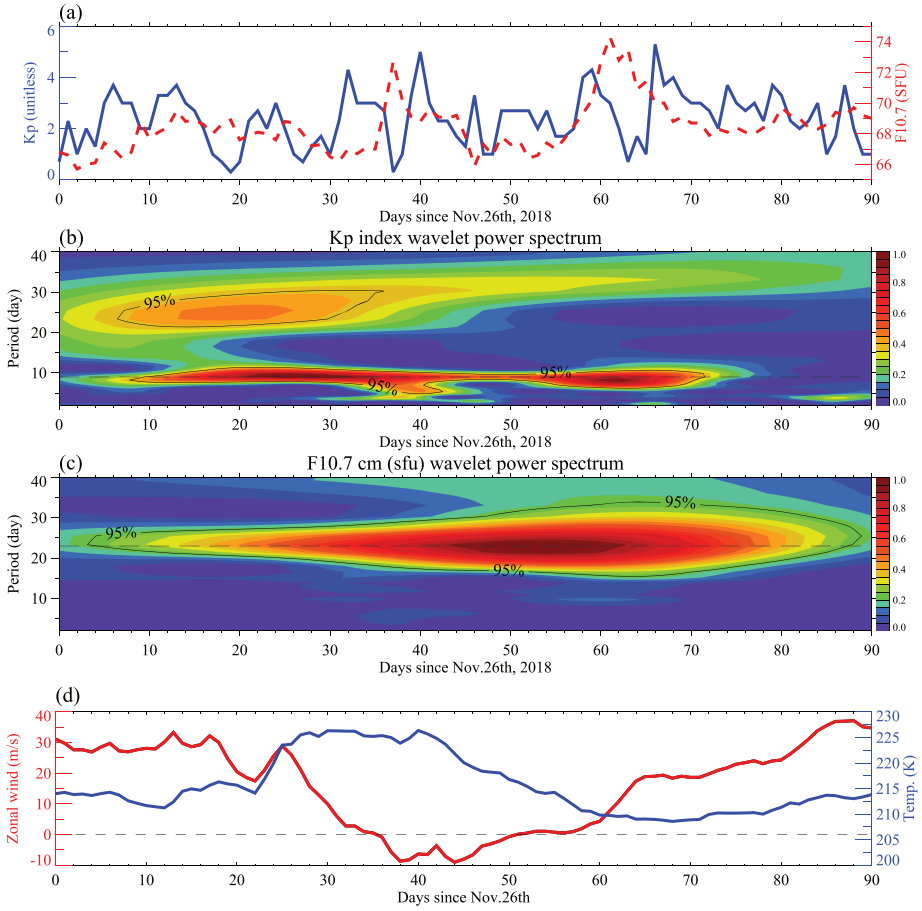

Figure 1. (a) Kp (blue) and F10.7 (red) indices between 26 November 2018 and 24 February 2019. The corresponding wavelet spectra of the (b) Kp and (c) F10.7-cm indices. (d) Daily zonal averaged zonal winds (red) and temperature (blue) at 30 km and 60°N. Dashed line denotes the period of 9 days in (b), 24 days in (c), and the zero winds in (d). Solid curve denotes the 95% significance level in panels (b) and (c).

Vergados et al., 2018) in the lower atmosphere could be responsible for the observed 60-day oscillation in brightness as well. However, the 60-day periodicity is beyond the scope of the current study. It is noticeable that the wavelet spectrum of the EOF1 time sequence, as shown in Figure 2f, suggested an 8–9-day oscillation on days ~ 10–30 (6–26 December 2018). We postulate that this periodicity was possibly due to the coincident fluctuations in geomagnetic activity, as illustrated in Figure 1b.

Figure 2g displays the latitudinal structure of the EOF2 in the GOLD data. Similar to the EOF1, the second largest principal component represented significant brightness changes in the EIA crest regions, but the variability was roughly opposite between the northern and southern hemispheres. It is noteworthy that the EOF2 (Figure 2h) showed a regular oscillating pattern with a period of ~16 days, as suggested by the wavelet spectrum in Figure 2i. Within the given time span, the Q16DO roughly had four cycles, and the absolute magnitude of the oscillation was greater between days 10–40 and subsequently decayed by ~60% after day 40. Since the quasi-16-day periodicity was not detected in the Kp and F10.7 indices, it was thus possibly tied to the waves arising in the troposphere and middle atmosphere. A closer look at the Q16DOs in the EIA crest regions is shown in Figure 3. The brightness anomaly (solid curves) was derived by subtracting the 20-day running means from the daily brightness in the northern (orange) and southern (blue) crests, which correspond to the bins of 5°–15° and −20°–10° magnetic latitudes, respectively. The percentage anomaly (dotted curves) was also calculated by normalizing the absolute anomaly to the 20-day running mean. The error bars indicate the random noise level. As expected, the anomalies exhibited 3–4 peaks and valleys, and the maxima brightness of the northern crest (solid orange curve) occurred near day 7, 22, 38, and 52,

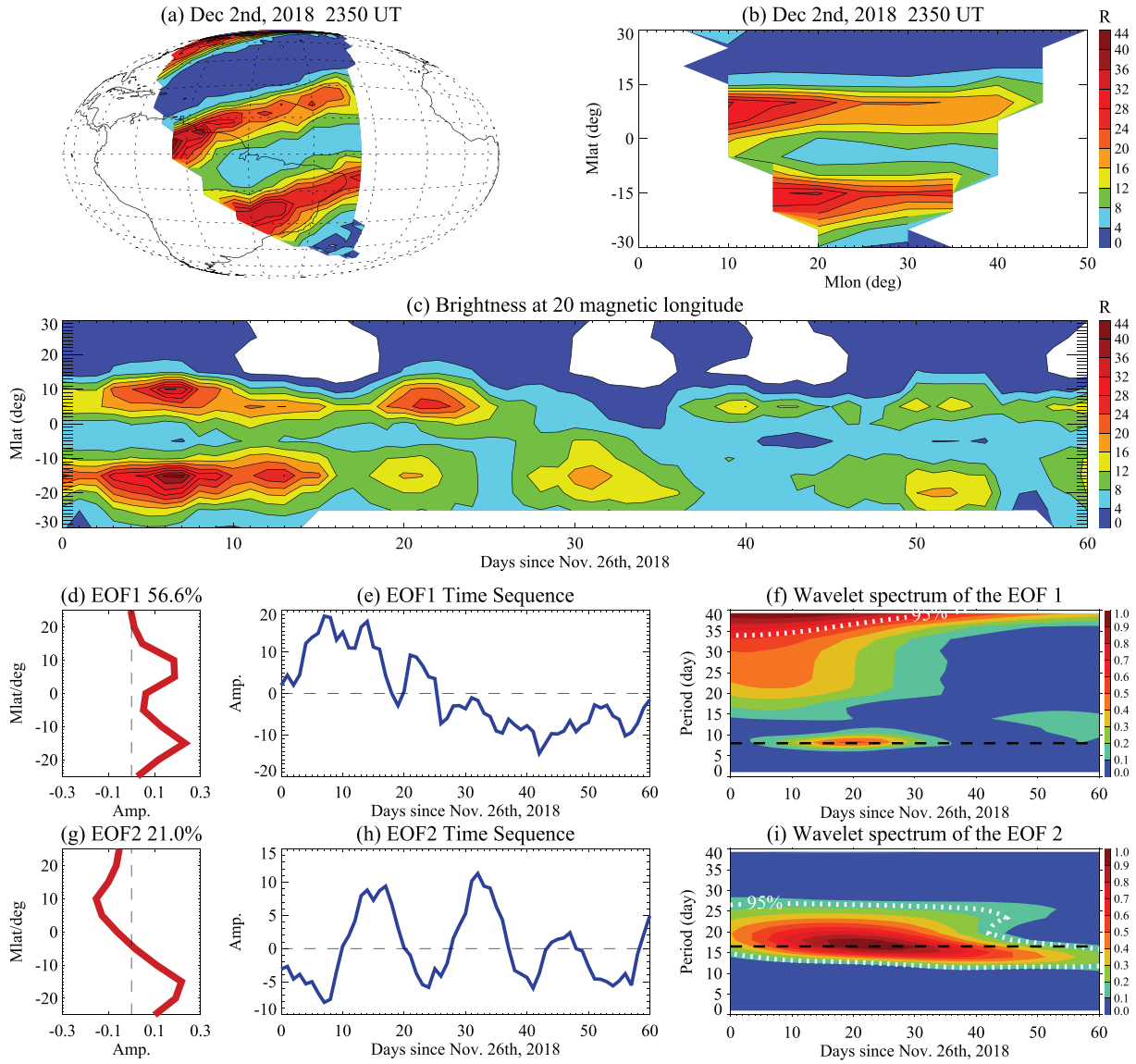

Figure 2. (a) GOLD image of OI 135.6-nm emission at 23:50 UT on day 2 December 2018. (b) The same image but smoothed by the 3° (lon) × 3° (lat) window in the magnetic coordinate system. (c) Magnetic latitude versus time brightness between 26 November 2018 and 25 January 2019. The latitudinal structure of the (d) first and (g) second principal components. (e) and (h) are the temporal variability of the EOF1 and EOF2, respectively. The wavelet spectra of the EOF1 and EOF2 time sequences are in (f) and (i). Black dashed line denotes the period of 9 and 16 days in (f) and (i), respectively. White dotted curve is the 95% significance level. White region in panel (a), (b), and (c) indicates the measurements are not available.

demonstrating a ~16-day oscillation which was aligned with the EOF2 in Figure 2. Also, the magnitude of the anomalies in the northern crest decreased from a peak value of 10 R on ~day 22 to 3 R on ~day 38, while the corresponding percentage anomalies increased from ~60% to 75%. The oscillation in the southern crest showed a similar overall decrease, but its magnitude appeared to be somewhat weaker than that in the northern counterpart. The significant decay in the absolute anomalies was possibly due to the overall deletion of brightness after day 25 (21 December 2018) as shown in Figure 2c.

A noteworthy point in Figure 3 is that the brightness anomalies were asymmetric (in antiphase between day 20 and day 50) between the southern and northern crests. Presumably, the Q16DO was induced by the E-region dynamo modulation due to tides and PWs, which has been widely proposed to account for the F-region ionosphere periodicities during the daytime in the context of geomagnetically and solar quiet conditions (e.g., England et al., 2010; Immel et al., 2006; Jin et al., 2008). If the coupling process is governed by symmetric E-region dynamo modulation, the resulting oscillations between the northern and southern

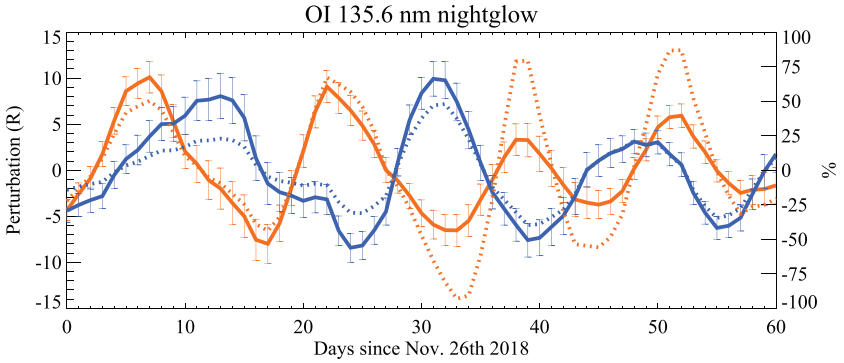

Figure 3. Daily absolute (solid) and percentage (dotted) anomalies of the OI 135.6-nm brightness, with respect to the 20-day running means, in the northern (orange) and southern (blue) crests of the EIA. Error bar on the top of absolute anomalies indicates random noise level.

crests would be more in-phase. The asymmetry, however, implies that the E-region dynamo modulation was not the exhaustive scenario in this case, which is not unexpected since the E-region dynamo effect (ExB) gradually fades away after the sunset. In other words, the E-region dynamo modulation may play a secondary role in transmitting the quasi-16-day periodicity into the F-region heights. Another candidate mechanism is the F_2-region in situ neutral winds, associated with the vertical penetration of tides and PWs, which drive the field-aligned motion of the plasma and produce the oscillations in electron densities. Using the first-principle modeling, Forbes et al. (2018) suggested this new mechanism to interpret the large-scale wave impacts on the ionosphere. However, to our best knowledge, there has been no observational proof to confirm this mechanism. Note that the EOF analysis also indicated the asymmetric oscillations in brightness between the northern and southern EIA crests (see Figure 2g).

Thus far, the Q16DOs in airglow have been established. We now turn to wave diagnostics in the mesosphere. Figure 4a displays the temperature anomalies as functions of longitude and time at 40°N and 80 km from SABER measurements. The time span is the same as that in Figures 2 and 3. The temperature anomalies were computed by subtracting the zonal mean temperature on a daily basis for ascending and descending portions of orbits separately (Gan et al., 2014). This algorithm effectively removes migrating tides and avoids tidal aliasing. In the mesosphere, the temperatures anomalies (Figure 4a) are characterized by a zonal wavenumber 1 structure. The wave pattern showed an obvious westward propagation during day 10–50 (6 December 2018 to 15 January 2019), after which the wave appeared to be stationary. The propagating wave component was significantly strengthened before the zonal wind reversal around day 35 (31 December 2018; see Figure 1d) since the dramatic change of zonal mean winds resulted in the changes to the refractive index and meridional gradient of potential vorticity, in favor of PW propagation and amplification (Charney & Drazin, 1961; Smith, 1983). Figure 4b illustrates the time series of temperature anomalies (blue curve) at 285°E longitude and its wavelet spectrum. This longitude sector is in the GOLD field of view. The red curve denotes the temperature anomalies derived by a 14–18-day bandpass filtering. In principle, the quasi-16-day perturbations were salient, and the peak wave magnitude of ~10 K occurred between day 25–35 (21–31 December). To further characterize the wave property, 2-D spectral analysis proposed by Salby (1982) was performed on the temperature anomalies (Figure 4c). It turns out that the quasi-16-day fluctuations had zonal wavenumber 1 and propagated westward, establishing a connection with the (1, −4) Rossby normal mode. Figure 4d further illustrates altitude versus latitude Q16DW magnitudes on day 25 (21 December 2018). From a global-scale perspective, the Q16DW showed a double-peak structure with a maximum magnitude of 12–14 K in the boreal stratosphere and mesosphere, as well as a localized peak of ~8 K at ~100 km in the Southern Hemisphere.

In regard to vertical coupling with the ionosphere, the Q16DW showed considerable complexity. Despite the observed Q16DW having a large vertical wavelength of approximately 70 km (the orange line in Figure 4d denotes the Q16DW phase structure at 50°N, where the magnitude maximized) in the boreal middle latitudes, its slow zonal phase speed (~18 m/s at 50°N) would result in quick wave dissipation, and thereby, a direct vertical penetration into the F-region heights was not anticipated. However, the

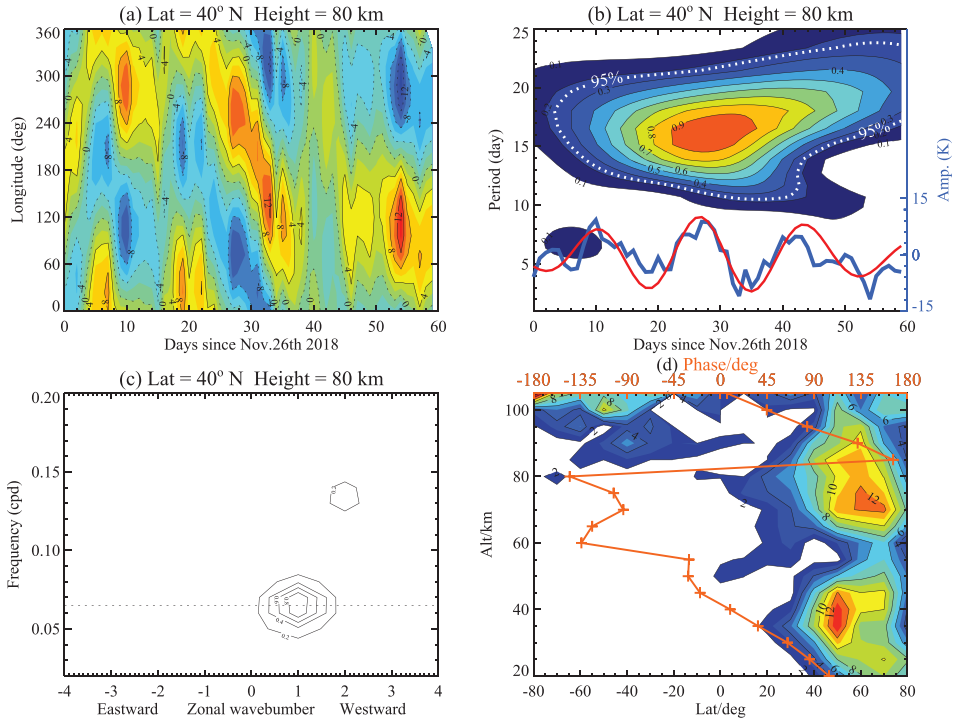

Figure 4. (a) Daily SABER temperature anomalies derived by subtracting the zonal means as functions of longitude and time at 40°N and 80 km. (b) The wavelet spectrum of the temperature anomalies at 285°E. The blue curve is the temperature anomalies at 285°E; the red curve denotes the least-squares fitting with a 16-day period. (c) The normalized frequency versus zonal wavenumber spectrum of the temperature anomalies in panel (a). Frequency is in cycle per day. Negative (positive) zonal wavenumber denotes eastward (westward) wave propagation. The dotted line denotes the period of 16 days. (d) The Q16DW magnitude as functions of altitude and latitude on day 25 (21 December 2018). Orange line denotes the altitudinal dependence of the Q16DW phase (in degree) at 50°N, where the magnitude maximizes.

large wave magnitude in both the mesosphere and stratosphere enabled the Q16DW to modulate tides, for example, the migrating semidiurnal tides (SW2). Those tidal components have been revealed to affect the ionosphere via direct penetration to the F-region heights (Pedatella et al., 2016; Pedatella & Maute, 2015). Also, as it is seen, the Q16DW may cross the equatorial region in the mesopause and lower thermosphere, accounting for the Q16DW in the Southern Hemisphere (Chandran et al., 2013; Day et al., 2011). Such a cross-equatorial behavior may lead to the wave momentum deposition into mean flows on a global scale, as well as the changes of circulation and constituent transport. All the above speculation merits a comprehensive investigation using the first-principle whole atmosphere models (for instance, the Whole Atmosphere Community Climate Model extended) in the near future.

4. Conclusions

The GOLD observations revealed prominent Q16DOs in the nighttime OI 135.6-nm emission over the EIA region during 26 November 2018 to 25 January 2019. Concurrently, SABER observed a Q16DW event at middle latitudes in the Northern Hemisphere, indicating that the Q16DW in the middle atmosphere was possibly the leading cause of the Q16DOs in the F-region ionosphere during this period. EOF analysis, along with a detailed examination of the temporal evolution of the brightness in the EIA crests, showed that the Q16DOs accounted for ~20% of the total brightness variability at around midnight. More importantly, the Q16DOs in the F-region ionosphere were asymmetric between the northern and southern crests. This asymmetry sheds light on the possible coupling mechanism. That is, other than modulating the E-region dynamo winds, the Q16DW-modulated tides possibly penetrate to the F-region heights and produce the Q16DOs in the field-aligned motion of the plasmas and thereby in electron densities during SSWs.

Acknowledgments

We appreciate Hanli Liu for the HAO internal review. QG and RE are supported by NASA contract 80GSFC18C006. WW is supported by NASA grants NNX14AE06G, NNX15AB83G, NNX16AH06G, NNX17AI42G, 80NSSC17K0013, and 80NSSC19K0278. LQ is supported by NASA grants NNX16AH06G and 80NSSC19K0278. NCAR is sponsored by the National Science Foundation. The Level 1C data used in this study is available at the GOLD Science Data Center (http://gold.cs.ucf.edu/search/) and at NASA's Space Physics Data Facility (http://spdf.gsfc.nasa.gov). The SABER data is freely accessed via the weblink (http://saber.gats-inc.com).

References

Akmaev, R. A. (2011). Whole atmosphere modeling: Connecting terrestrial and space weather. *Reviews of Geophysics*, *49*. https://doi.org/10.1029/2011rg000364

Altadill, D. (2000). Planetary wave type oscillations in the ionospheric F region. *Middle Atmosphere and Lower Thermosphere Electrodynamics*, *26*(8), 1287–1296. https://doi.org/10.1016/s0273-1177(00)00120-4

Borries, C., & Hoffmann, P. (2010). Characteristics of F2-layer planetary wave-type oscillations in northern middle and high latitudes during 2002 to 2008. *Journal of Geophysical Research*, *115*, 9. https://doi.org/10.1029/2010JA015456

Chandran, A., Garcia, R. R., Collins, R. L., & Chang, L. C. (2013). Secondary planetary waves in the middle and upper atmosphere following the stratospheric sudden warming event of January 2012. *Geophysical Research Letters*, *40*(9), 1861–1867. https://doi.org/10.1002/grl.50373

Chang, L. C., Palo, S. E., & Liu, H. L. (2011). Short-term variability in the migrating diurnal tide caused by interactions with the quasi 2 day wave. *Journal of Geophysical Research*, *116*, 18. https://doi.org/10.1029/2010JD014996

Chang, L. C., Palo, S. E., Liu, H. L., Fang, T. W., & Lin, C. S. (2010). Response of the thermosphere and ionosphere to an ultra fast Kelvin wave. *Journal of Geophysical Research*, *115*, A00G40. https://doi.org/10.1029/2010JA015453

Chang, L. C., Yue, J., Wang, W. B., Wu, Q., & Meier, R. R. (2014). Quasi two day wave-related variability in the background dynamics and composition of themesosphere/thermosphere and the ionosphere. *Journal of Geophysical Research: Space Physics*, *119*, 4786–4804. https://doi.org/10.1002/2014JA019936

Charney, J. G., & Drazin, P. G. (1961). Propagation of planetary scale disturbances from the lower to the upper atmosphere. *Journal of Geophysical Research*, *66*, 83–109.

Day, K. A., Hibbins, R. E., & Mitchell, N. J. (2011). Aura MLS observations of the westward-propagating s=1, 16-day planetary wave in the stratosphere, mesosphere and lower thermosphere. *Atmospheric Chemistry and Physics*, *11*(9), 4149–4161. https://doi.org/10.5194/acp-11-4149-2011

Eastes, R. W., McClintock, W. E., Burns, A. G., Anderson, D. N., Andersson, L., Codrescu, M., et al. (2017). The Global-Scale Observations of the Limb and Disk (GOLD) Mission. *Space Science Reviews*, *212*(1–2), 383–408. https://doi.org/10.1007/s11214-017-0392-2

Eastes, R. W., Solomon, S. C., Daniell, R. E., Anderson, D. N., Burns, A. G., England, S. L., et al. (2019). Global-scale observations of the equatorial ionization anomaly. *Geophysical Research Letters*, *46*, 9318–9326. https://doi.org/10.1029/2019GL084199

England, S. L., Immel, T. J., Huba, J. D., Hagan, M. E., Maute, A., & DeMajistre, R. (2010). Modeling of multiple effects of atmospheric tides on the ionosphere: An examination of possible coupling mechanisms responsible for the longitudinal structure of the equatorial ionosphere. *Journal of Geophysical Research*, *115*, A05308. https://doi.org/10.1029/2009JA014894

Forbes, J. M. (1996). Planetary waves in the thermosphere-ionosphere system. *Journal of Geomagnetism and Geoelectricity*, *48*(1), 91–98. https://doi.org/10.5636/jgg.48.91

Forbes, J. M., Hagan, M. E., Miyahara, S., Vial, F., Manson, A. H., Meek, C. E., & Portnyagin, Y. I. (1995). Quasi 16-day oscillation in the mesosphere and lower thermosphere. *Journal of Geophysical Research*, *100*(D5), 9149–9163. https://doi.org/10.1029/94JD02157

Forbes, J. M., & Leveroni, S. (1992). Quasi 16-day oscillation in the ionosphere. *Geophysical Research Letters*, *19*(10), 981–984. https://doi.org/10.1029/92gl00399

Forbes, J. M., Maute, A., Zhang, X., & Hagan, M. E. (2018). Oscillation of the ionosphere at planetary-wave periods. *Journal of Geophysical Research:Space Physics*, *123*, 7634–7649. https://doi.org/10.1029/2018JA025720

Forbes, J. M., Palo, S. E., & Zhang, X. L. (2000). Variability of the ionosphere. *Journal of Atmospheric and Solar-Terrestrial Physics*, *62*(8), 685–693. https://doi.org/10.1016/S1364-6826(00)00029-8

Gan, Q., Du, J., Ward, W. E., Beagley, S. R., Fomichev, V. I., & Zhang, S. D. (2014). Climatology of the diurnal tides from eCMAM30 (1979 to 2010) and its comparison with SABER. *Earth Planets and Space*, *66*(1), 1–24. https://doi.org/10.1186/1880-5981-66-103

Gan, Q., Eastes, R. W., Burns, A. G., Wang, W., Qian, L., Solomon, S. C., et al. (2020). First synoptic observations of geomagnetic storm effects on the global-scale OI 135.6-nm dayglow in the thermosphere by the GOLD mission. *Geophysical Research Letters*, *47*, e2019GL085400. https://doi.org/10.1029/2019GL085400

Gan, Q., Oberheide, J., & Pedatella, N. M. (2018). Sources, sinks, and propagation characteristics of the quasi 6-day wave and its impact on the residual mean circulation. *Journal of Geophysical Research:Atmospheres*, *123*, 9152–9170. https://doi.org/10.1029/2018JD028553

Gan, Q., Oberheide, J., Yue, J., & Wang, W. (2017). Short-term variability in the ionosphere due to the nonlinear interaction between the 6-day wave and migrating tides. *Journal of Geophysical Research: Space Physics*, *122*, 8831–8846. https://doi.org/10.1002/2017JA023947

Gan, Q., Wang, W., Yue, J., Liu, H., Chang, L. C., Zhang, S., et al. (2016). Numerical simulation of the 6 day wave effects on the ionosphere: Dynamo modulation. *Journal of Geophysical Research: Space Physics*, *121*, 10,103–10,116. https://doi.org/10.1002/2016JA022907

Gan, Q., Yue, J., Chang, L. C., Wang, W. B., Zhang, S. D., & Du, J. (2015). Observations of thermosphere and ionosphere changes due to the dissipative 6.5-day wave in the lower thermosphere. *Annales Geophysicae*, *33*(7), 913–922. https://doi.org/10.5194/angeo-33-913-2015

Immel, T. J., Sagawa, E., England, S. L., Henderson, S. B., Hagan, M. E., Mende, S. B., et al. (2006). Control of equatorial ionospheric morphology by atmospheric tides. *Geophysical Research Letters*, *33*, L15108. https://doi.org/10.1029/2006GL026161

Jin, H., Miyoshi, Y., Fujiwara, H., & Shinagawa, H. (2008). Electrodynamics of the formation of ionospheric wave number 4 longitudinal structure. *Journal of Geophysical Research*, *113*, 7. https://doi.org/10.1029/2008JA013301

Lastovicka, J. (2006). Forcing of the ionosphere by waves from below. *Journal of Atmospheric and Solar-Terrestrial Physics*, *68*(3–5), 479–497. https://doi.org/10.1016/j.jastp.2005.01.018

Lei, J. H., Thayer, J. P., Forbes, J. M., Wu, Q., She, C. L., Wan, W. X., & Wang, W. B. (2008). Ionosphere response to solar wind high-speed streams. *Geophysical Research Letters*, *35*, 5. https://doi.org/10.1029/2008gl035208

Liu, H. L. (2016). Variability and predictability of the space environment as related to lower atmosphere forcing. *Space Weather-the International Journal of Research and Applications*, *14*(9), 634–658. https://doi.org/10.1002/2016sw001450

Liu, H. L., & Roble, R. G. (2002). A study of a self-generated stratospheric sudden warming and its mesospheric-lower thermospheric impacts using the coupled TIME-GCM/CCM3. *Journal of Geophysical Research*, *107*(D23), ACL 15-1–ACL 15-18. https://doi.org/10.1029/2001JD001533

Liu, H. L., Wang, W., Richmond, A. D., & Roble, R. G. (2010). Ionospheric variability due to planetary waves and tides for solar minimum conditions. *Journal of Geophysical Research*, *115*. https://doi.org/10.1029/2009JA015188

Mendillo, A., Rishbeth, H., Roble, R. G., & Wroten, J. (2002). Modelling F2-layer seasonal trends and day-to-day variability driven by coupling with the lower atmosphere. *Journal of Atmospheric and Solar-Terrestrial Physics*, *64*(18), 1911–1931. https://doi.org/10.1016/s1364-6826(02)00193-1

Meyer, C. K. (1999). Gravity wave interactions with mesospheric planetary waves: A mechanism for penetration into the thermosphere-ionosphere system. *Journal of Geophysical Research*, *104*(A12), 28,181–28,196. https://doi.org/10.1029/1999JA900346

Oberheide, J., Pedatella, N. M., Gan, Q., Kumari, K., Burns, A. G., & Eastes, R. (2020). Thermosphere composition O/N_2 response to an altered meridional mean circulation during sudden stratospheric warmings observed by GOLD. *Geophysical Research Letters*, *47*, e2019GL086313. https://doi.org/10.1029/2019GL086313

Oberheide, J., Shiokawa, K., Gurubaran, S., Ward, W. E., Fujiwara, H., Kosch, M. J., & Takahashi, H. (2015). The geospace response to variable inputs from the lower atmosphere: A review of the progress made by task group 4 of CAWSES-II. *Progress in Earth and Planetary Science*, *2*(1), 1–31. https://doi.org/10.1186/s40645-014-0031-4

Pedatella, N. M., & Forbes, J. M. (2009). Modulation of the equatorial F-region by the quasi-16-day planetary wave. *Geophysical Research Letters*, *36*. https://doi.org/10.1029/2009gl037809

Pedatella, N. M., & Forbes, J. M. (2012). The quasi 2 day wave and spatial-temporal variability of the OH emission and ionosphere. *Journal of Geophysical Research*, *117*, 1320. https://doi.org/10.1029/2011JA017186

Pedatella, N. M., Lei, J., Thayer, J. P., & Forbes, J. M. (2010). Ionosphere response to recurrent geomagnetic activity: Local time dependency. *Journal of Geophysical Research*, *115*, 8. https://doi.org/10.1029/2009JA014712

Pedatella, N. M., & Maute, A. (2015). Impact of the semidiurnal lunar tide on the midlatitude thermospheric wind and ionosphere during sudden stratosphere warmings. *Journal of Geophysical Research:Space Physics*, *120*, 10,740–10,753. https://doi.org/10.1002/2015JA021986

Pedatella, N. M., Richmond, A. D., Maute, A., & Liu, H. L. (2016). Impact of semidiurnal tidal variability during SSWs on themean state of the ionosphere and thermosphere. *Journal of Geophysical Research:Space Physics*, *121*, 8077–8088. https://doi.org/10.1002/2016JA022910

Qian, L. Y., Burns, A. G., Solomon, S. C., & Wang, W. B. (2013). Annual/semiannual variation of the ionosphere. *Geophysical Research Letters*, *40*(10), 1928–1933. https://doi.org/10.1002/grl.50448

Remsberg, E. E., Marshall, B. T., Garcia-Comas, M., Krueger, D., Lingenfelser, G. S., Martin-Torres, J., et al. (2008). Assessment of the quality of the Version 1.07 temperature-versus-pressure profiles of the middle atmosphere from TIMED/SABER. *Journal of GeophysicalResearch*, *113*, D17101. https://doi.org/10.1029/2008JD010013

Richmond, A. D. (1995). Ionospheric electrodynamics using magnetic apex coordinates. *Journal of Geomagnetism and Geoelectricity*, *47*(2), 191–212. https://doi.org/10.5636/jgg.47.191

Rishbeth, H., & Mendillo, M. (2001). Patterns of F2-layer variability. *Journal of Atmospheric and Solar-Terrestrial Physics*, *63*(15), 1661–1680. https://doi.org/10.1016/S1364-6826(01)00036-0

Salby, M. L. (1981). Rossby normal-modes in nonuniform background configurations. Part II. Equinox and solstice conditions. *Journal of the Atmospheric Sciences*, *38*(9), 1827–1840. https://doi.org/10.1175/1520-0469(1981)038<1827:Rnminb>2.0.Co;2

Salby, M. L. (1982). Sampling theory for asynoptic satellite observations. Part I: Space-time spectra, resolution, and aliasing. *Journal of the Atmospheric Sciences*, *39*, 2577–2600. https://doi.org/10.1175/1520-0469(1982)039<2577:STFASO>2.0.CO;2

Salby, M. L. (1984). Survey of planetary-scale traveling waves—The state of theory and observations. *Reviews of Geophysics*, *22*(2), 209–236. https://doi.org/10.1029/RG022i002p00209

Sassi, F., McCormack, J. P., & McDonald, S. E. (2019). Whole atmosphere coupling on intraseasonal and interseasonal time scales: A potential source of increased predictive capability. *Radio Science*. https://doi.org/10.1029/2019rs006847

Shepherd, G. G., Stegman, J., Espy, P., McLandress, C., Thuillier, G., & Wiens, R. H. (1999). Springtime transition in lower thermospheric atomic oxygen. *Journal of Geophysical Research*, *104*(A1), 213–223. https://doi.org/10.1029/98JA02831

Smith, A. K. (1983). Stationary waves in the winter stratosphere: Seasonal and interannual variability. *Journal of the Atmospheric Sciences*, *40*(1), 245–261.

Vergados, P., Liu, G., Mannucci, A. J., & Janches, D. (2018). Equatorial intraseasonal temperature oscillations in the lower thermosphere from SABER. *Geophysical Research Letters*, *45*(20), 10,893–10,902. https://doi.org/10.1029/2018gl079467

Vincent, R. A. (2015). The dynamics of the mesosphere and lower thermosphere: A brief review. *Progress in Earth and Planetary Science*, *2*(1), 1–13. https://doi.org/10.1186/s40645-015-0035-8

Yamazaki, Y., Stolle, C., Matzka, J., & Alken, P. (2018). Quasi-6-day wave modulation of the equatorial Electrojet. *Journal of Geophysical Research:Space Physics*, *123*, 4094–4109. https://doi.org/10.1029/2018JA025365

Yi, L., & Chen, P. R. (1993). Long-period oscillations in the equatorial ionization anomaly correlated with the neutral wind in the mesosphere. *Journal of Atmospheric and Terrestrial Physics*, *55*(10), 1317–1323. https://doi.org/10.1016/0021-9169(93)90100-d

Yue, J., & Wang, W. B. (2014). Changes of thermospheric composition and ionospheric density caused by quasi 2 day wave dissipation. *Journal of Geophysical Research:Space Physics*, *119*, 2069–2078. https://doi.org/10.1002/2013JA019725

Yue, J., Wang, W. B., Richmond, A. D., Liu, H. L., & Chang, L. C. (2013). Wavenumber broadening of the quasi 2 day planetary wave in the ionosphere. *Journal of Geophysical Research:Space Physics*, *118*, 3515–3526. https://doi.org/10.1002/jgra.50307

Yue, J., Wang, W. B., Ruan, H. B., Chang, L. C., & Lei, J. H. (2016). Impact of the interaction between the quasi-2 day wave and tides on the ionosphere and thermosphere. *Journal of Geophysical Research:Space Physics*, *121*, 3555–3563. https://doi.org/10.1002/2016JA022444